# Astrometry of 6.7 GHz Methanol Maser toward W 3(OH) with Japanese VLBI Network

Naoko Matsumoto,[1,2] Mareki Honma,[1,2] Yasuko Isono,[3] Hideki Ujihara,[4] Kimihiro Kimura,[5]
Kouhei Matsumoto,[5] Satoko Sawada-Satoh,[6] Akihiro Doi,[7] Kenta Fujisawa,[8] and Yuji Ueno[6]

[1]*Department of Astronomical Science, The Graduate University of Advanced Studies (SOKENDAI), 2-21-1 Osawa, Mitaka, Tokyo 181-8588*
*naoko.matsumoto@nao.ac.jp*

[2]*Mizusawa VLBI Observatory, National Astronomical Observatory of Japan, 2-21-1 Osawa, Mitaka, Tokyo 181-8588*

[3]*Solar-Terrestrial Environment Laboratory, Nagoya University, Furo-cho, Chikusa-ku, Nagoya 464-8601*

[4]*Space-Time Standards Group, Kashima Space Research Center National Institute of Information and Communications Technology,*
*893-1 Hirai, Kashima, Ibaraki 314-0012*

[5]*Department of Physical Science, Osaka Prefecture University, 1-1 Gakuen-cho, Naka-ku, Sakai 599-8231*

[6]*Mizusawa VLBI Observatory, National Astronomical Observatory of Japan, 2-12 Hoshigaoka, Mizusawa-ku, Oshu, Iwate 023-0861*

[7]*Institute of Space and Astronautics, Japan Aerospace Exploration Agency, 3-1-1 Yoshinodai, Chuo-ku, Sagamihara 252-5210*

[8]*Faculty of Science, Yamaguchi University, 1677-1 Yoshida, Yamaguchi, Yamaguchi 753-8512*

## Abstract

We present the results of multiepoch VLBI observations for a 6.7 GHz methanol maser toward the UC H II region of W 3(OH) with Japanese VLBI Network (JVN). Based on phase-referencing VLBI astrometry, we derived the trigonometric annual parallax to be $0.598 \pm 0.067$ mas, corresponding to a distance of $1.67^{+0.21}_{-0.17}$ kpc. This is the first detection of parallax for a 6.7 GHz methanol maser with JVN, and demonstrates that JVN/VERA is capable of conducting VLBI astrometry for 6.7 GHz methanol maser sources within few kpc from the Sun. Based on in-beam mapping of the W 3(OH) methanol maser, we also measured the internal proper motions of its 6.7 GHz methanol maser for the first time. The internal proper motions basically show north–south expansion with a velocity of few $km\,s^{-1}$, being similar to OH masers. The spatial distribution and the internal proper motions of 6.7 GHz methanol masers suggest a rotating and expanding torus structure surrounding the UC H II region.

**Key words:** astrometry — ISM: individual (Westerhout 3(OH)) — masers — stars: distances — stars: kinematics

## 1. Introduction

Sources of 6.7 GHz methanol maser are potential targets of VLBI astrometry to trace the 3-D structure of the Galaxy. Recently Rygl et al. (2010) reported the first parallax measurements of 6.7 GHz methanol maser sources with European VLBI Network (EVN), showing that this maser line can also be used for VLBI astrometry. The 6.7 GHz methanol maser line is the brightest among the methanol maser emissions, and nearly a thousand of 6.7 GHz methanol maser sources has been discovered in the Galactic plane (e.g., Green et al. 2009). In addition, the internal proper motions of the methanol maser, itself, are generally smaller than those of $H_2O$ masers, and structures of maser components are stable for the period required for astrometric monitoring (1 yr or more). In order to conduct VLBI astrometry of 6.7 GHz methanol masers, we installed C-band receivers on VERA (VLBI Exploration of Radio Astrometry) antennas, and started test observations with some Japanese VLBI Network (JVN) stations that are also operating at 6.7 GHz. Among them, we conducted a phase-referencing observation of W 3(OH) to evaluate the astrometric capability of JVN/VERA. W 3(OH) is one of the brightest 6.7 GHz methanol maser sources that have been extensively studied, and an accurate distance has already been reported (Xu et al. 2006; Hachisuka et al. 2006). Hence, W 3(OH) is

one of the best targets to investigate the astrometric capability of the JVN/VERA array.

W 3(OH) is a massive star-forming region located in the Perseus arm at a distance of $1.95 \pm 0.04$ kpc (Xu et al. 2006). W 3(OH) is the UC H II region associated with a far-infrared source with a total luminosity of $10^5 L_\odot$ (Campbell et al. 1989; Harper 1974), which corresponds to the luminosity of a main-sequence star of spectral class O7 (Dreher & Welch 1981). The exciting star was detected by a Chandra X-Ray observation (Feigelson & Townsley 2008), and its coordinates were determined to be $\alpha_{J2000.0} = 02^h27^m03\overset{s}{.}84$, $\delta_{J2000.0} = +61°52'24\overset{''}{.}9$ with a position error of $0\overset{''}{.}4$. The UC H II region, itself, is a limb-brightened shell with a diameter of $\sim 10^3$ AU, which was measured at 15 GHz (Dreher & Welch 1981). The expansion of the UC H II region was detected by Kawamura and Masson (1998) with a typical expansion speed of $3–5\,km\,s^{-1}$. In the western part of this UC H II region, various maser emissions were detected: 12 GHz methanol maser (Moscadelli et al. 1999, 2002, 2010; Xu et al. 2006), 6.7 GHz methanol maser (Harvey-Smith & Cohen 2006; Etoka et al. 2005; Menten et al. 1992), 1.6/1.7/4.7/6/13 GHz OH masers (Fish & Sjouwerman 2007; Fish et al. 2006; Harvey-Smith & Cohen 2006; Wright et al. 2004a, 2004b; Desmurs et al. 1998; Baudry et al. 1998; Bloemhof et al. 1992; Norris et al. 1982). In contrast, only a few maser components were found in

the eastern part of the UC H II region (Fish & Sjouwerman 2007). Eight GHz OH emission and absorption lines (Baudry et al. 1993) and ammonia absorption line (Reid et al. 1987; Guilloteau et al. 1983) were also observed in the western part of this region. From these observations, several models were proposed based on previous studies; for instance, a torus model (Fish & Sjouwerman 2007; Dickel & Goss 1987; Guilloteau et al. 1983), a disk model (Moscadelli et al. 2010; Wright et al. 2004a), an expansion or cometary bow-shock model (Bloemhof et al. 1992), and a collapsing envelope (Reid et al. 1980). To test these models, high-resolution images and three-dimensional velocity structure are needed as among important approaches.

In this paper, we report on the results of VLBI observations of the 6.7 GHz methanol maser of W 3(OH) with JVN/VERA. We present the distributions and internal motions of this maser obtained with in-beam VLBI imaging, and also the results of phase-referencing astrometry.

## 2. Observations and Data Analysis

### 2.1. Observations

We observed a 6.7 GHz methanol maser emission toward W 3(OH) ($\alpha_{J2000.0} = 02^h27^m03^s.81920$, $\delta_{J2000.0} = +61°52'25''.2300$: Xu et al. 2006) from 2008 May to 2010 April with JVN including VERA. Table 1 summarizes these observations. We conducted one-beam switching observations, because all 6.7 GHz receiving systems are single-beam in JVN as well as VERA. In the present observations, therefore, W 3(OH) and a phase-reference source, J0244+6228 [2°.17 from W 3(OH), $\alpha_{J2000.0} = 02^h44^m57^s.69667$, $\delta_{J2000.0} = +62°28'06''.5155$, ICRF], were alternately observed with 5 min cycles (typically 2 and 1.8 min on-source integration times for W 3(OH) and J0244+6228, and the rest for slewing). 3C 84 was also observed once an hour as a calibrator. A radio frequency of 6.668518 GHz is chosen in this paper as the rest frequency of CH$_3$OH $5_1 \rightarrow 6_0 A^+$ transition. Left-hand circular polarization was received, except at Iriki and Ogasawara stations at epochs 1 and 2, in which linear polarization receivers were used. The received signals were filtered in a 16 MHz bandwidth channel (epochs 1–3), or 16 channels with 16 MHz bandwidth each (epochs 4–6). Filtered signals

were recorded with a SONY DIR1000 recorder at a rate of 128 Mbit s$^{-1}$ (epochs 1–3) or DIR2000 recorder at a rate of 1024 Mbit s$^{-1}$ (epochs 4–6). The recorded signals were correlated with the Mitaka FX correlator (Chikada et al. 1991). Since the maser line is narrow, and the phase-reference source is bright enough, we selected a small portion of bandwidth (4 MHz for epochs 1–3 or 8 MHz for epochs 4–6) centered at the maser line in the correlation process to obtain high spectral resolution. This produced auto-correlation and cross-correlation spectra consisting of 1024 spectral channels with a frequency spacing of 3.91 kHz ($\sim 0.18$ km s$^{-1}$) for epochs 1–3, and 512 spectral channels with a frequency spacing of 15.63 kHz ($\sim 0.70$ km s$^{-1}$) for epochs 4–6.

### 2.2. In-Beam and Phase-Referencing Mappings

In this paper, we produced two types of maser maps: one is an in-beam map for researching internal maser proper motions with respect to a reference maser component, and the other is a phase-referencing map for measuring absolute positions with respect to a phase-reference source.

In both mappings, data reduction was performed using the NRAO AIPS package, basically in a standard manner. The delay and the delay-rate offset were calibrated measuring 3C 84. The bandpass responses were also calibrated using 3C 84. Amplitude calibrations were performed by a template method with the total-power spectra of W 3(OH). For data from the Iriki and Ogasawara stations in epochs 1 and 2, we also applied special amplitude calibrations to corrections of the polarization difference (linear/circular) using a method described in Sugiyama et al. (2008b).

For in-beam mapping, fringe-fitting was conducted for a reference maser component of $v_{LSR} = -45.4$ km s$^{-1}$ in W 3(OH), which is the brightest component in a W 3(OH) methanol maser in our data. In self-calibration of the reference maser component, models of clean components were made with the DIFMAP software package provided by Caltech to obtain faint components of the maser emission from the reference maser component. The solutions of the self-calibration were applied to other velocity channels of the maser data.

For phase-referencing mapping, instead of the reference maser component, fringe solutions were obtained for J0244+6228 with solution intervals of one minute. Solutions

**Table 1.** Summary of JVN observations.

| Epoch | Date YYYY/DOY | Duration [UT] | Telescope* | Synthesized beam[†] (mas, °) |
|---|---|---|---|---|
| 1[§] | 2008/131 | 22:00–29:00 | M, R,[‡] S, O,[‡] Y, U | 5.6 × 3.2, −33.5 |
| 2[§] | 2008/301 | 13:00–18:00 | M, R,[‡] S, O,[‡] Y, U | 6.1 × 3.1, −38.4 |
| 3[§] | 2009/143 | 23:05–31:00 | M, R, S, O, Y | 4.5 × 2.8, −58.0 |
| 4 | 2009/338 | 08:15–16:23 | M, R, S, O | 4.2 × 2.6, −24.0 |
| 5 | 2010/046 | 03:30–11:38 | M, R, S, O | 3.8 × 2.6, −35.2 |
| 6 | 2010/102 | 23:44–31:53 | M, R, S, O | 3.6 × 2.7, −35.1 |

* Telescope code. M: VERA telescope at Mizusawa station; R: Iriki (VERA); S: Ishigaki (VERA); O: Ogasawara (VERA); Y: Yamaguchi; U: Usuda.
[†] Synthesized beam size and position angle.
[‡] The received signal was linear polarization.
[§] The velocity channel resolution of visibility data is 3.91 kHz at these epochs, and 15.63 kHz at other epochs.

of self-calibration were also obtained for J0244+6228. In the self-calibration, J0244+6228 had no distinct structure in any epoch, and its peak flux was $\sim 0.6$–$1\,\mathrm{Jy\,beam^{-1}}$. Solutions of the self-calibration for J0244+6228 were applied to data of W 3(OH). Since the apriori delay model used in the correlator was not accurate enough for VLBI astrometry, we recalculated more precise delays and made corrections for the differences between them. The difference in the optical path length was $\sim 2\,\mathrm{mm}$, or less, between our recalculated model and the CALC9 model developed by the NASA/GSFC VLBI group. In this correction, the visibility phase errors caused by tropospheric delays were calibrated based on GPS measurements (Honma et al. 2008). The ionospheric delay was also calibrated based on the data of the total vertical electron content produced by JPL.

Synthesis imaging and deconvolution were performed using the AIPS task IMAGR with uniform weighting. The synthesized beam sizes (FWHM) and position angles are listed in table 1. Both kinds of map were made with $8192\,\mathrm{pix} \times 8192\,\mathrm{pix}$ and its pixel size is $0.5\,\mathrm{mas\,pix^{-1}}$. When we made the phase-referencing maps, for epochs 1–3, every four velocity channels were combined into one to make a velocity resolution equal through all six epochs, because we used different data for velocity resolution in epochs 1–3 and 4–6. For in-beam maps, there was no need to combine channels into phase-referencing maps because we used only data with the same velocity resolution in epochs 1–3. Finally, the maser positions were derived by Gaussian fittings using the AIPS task JMFIT for both kinds of maps.

### 2.3. Derivation of Internal Proper Motions

To investigate the maser distribution and the internal proper motion, we used in-beam maps of epochs 1–3. This is because epochs 4–6 did not include antennas with large apertures, such as Yamaguchi 32 m and Usuda 64 m, and hence the number of detected components decreased drastically compared to epochs 1–3. All maser components whose signal-to-noise ratios are larger than 10 were used for the measurement of internal proper motions. We identified maser components with the same velocity within a beam size ($\theta_{\mathrm{beam}}$) between epochs, because the proper motion of the methanol maser was expected to be small. In fact, most of the components were identified within a separation of 1 mas. For maser components identified at all three epochs, we used the least-squares method for fitting the linear proper motion to position-time data sets with equal-weighting. In the present study, the minimum proper motion which we could detect is roughly estimated to be $0.1\theta_{\mathrm{beam}}/\Delta t_{\mathrm{obs}}$, which is $\sim 0.58\,\mathrm{mas\,yr^{-1}}$ or $\sim 5.4\,\mathrm{km\,s^{-1}}$ using the distance of 1.95 kpc. $\Delta t_{\mathrm{obs}}$ is a maximum time span of observations, which is 378 d between epochs 1 and 3. The value of 0.1 is equal to the reciprocal of the lowest signal-to-noise ratio of 10 in our map. The signal-to-noise ratio typically ranged over $\sim 10$–150 in our results.

### 2.4. Derivation of Annual Parallax and Absolute Proper Motion

Using the phase-referenced maps, we obtained absolute proper motions of 6.7 GHz maser components toward W 3(OH) with respect to the extragalactic source of

J0244+6228. Finally, five maser components were selected to derive an annual parallax and the absolute proper motions based on the following conditions. Each maser component has the same systemic velocity, apparently similar structure, and is present throughout all epochs. These five maser components have signal-to-noise ratios greater than 10. Three of the five components were considered to have the same maser feature, which means that maser emissions were stimulated in the same gas clump. This is because the positions of these three maser components are located within a beam size, and their systemic velocities are adjacent. We adopted the most conservative approach of assuming 100% correlation in three of the maser components. The two other maser components were considered to be independent. Thus, five maser components correspond to three maser features. The absolute motion of each maser component could be modeled by the sum of a linear proper motion and an annual parallax. In this astrometric analysis, we assumed that all of the maser components have the same annual parallax, and we simultaneously determined their proper motions and initial positions in right ascension and declination along with the common annual parallax by a least-squares method for analyzing the five maser components. When the common annual parallax and the proper motion of each component were estimated simultaneously, these three maser features were assumed to have the same error bars, which were determined so that the reduced $\chi^2$ would become unity. Thus, the error bars of each position of the three maser components sharing the same feature were enlarged by a factor of $\sqrt{3}$ compared to the two other components. After subtracting the fitting results of an annual parallax, proper motions of each maser component were also estimated with equal weight by the least-squares method. The averaged proper motions of the three features were also estimated.

## 3. Results

### 3.1. Spatial Distribution and Internal Proper Motions

The numbers of components detected in the in-beam map were 129 at epoch 1, 135 at epoch 2, and 149 at epoch 3. Figure 1 and table 2 show the spatial and velocity distributions of the 6.7 GHz methanol maser components at epoch 2 along with the integral flux intensity. The absolute position of the maser component with $v_{\mathrm{LSR}} = -45.4\,\mathrm{km\,s^{-1}}$ at (0, 0) coordinates in figure 1 (301 DOY in 2008) is $\alpha_{\mathrm{J2000.0}} = 02^{\mathrm{h}}27^{\mathrm{m}}03\overset{\mathrm{s}}{.}8178 \pm 0\overset{\mathrm{s}}{.}0080$, $\delta_{\mathrm{J2000.0}} = 61°52'25''\!.24824 \pm 0''\!.00049$, which was obtained from the absolute astrometry with respect to J0244+6228 (see subsection 3.2). This error is dominated by the position accuracy of phase-reference source J0244+6228 in the ICRF catalog. In figure 1, 15 GHz radio continuum in Bloemhof, Reid, and Moran (1992) was superimposed by using the methanol and OH maser coordinates in figure 6 in Bloemhof, Reid, and Moran (1992). The ionizing star position from Feigelson and Townsley (2008) was also plotted.

We found seven clusters, denoted as clusters A–G in figure 1. The radial velocity of the components ranges from $v_{\mathrm{LSR}} = -41.5$ to $-48.9\,\mathrm{km\,s^{-1}}$. The red-shifted components are in the south part (clusters D–G), and blue-shifted are in the north (clusters A–C). These seven clusters of maser
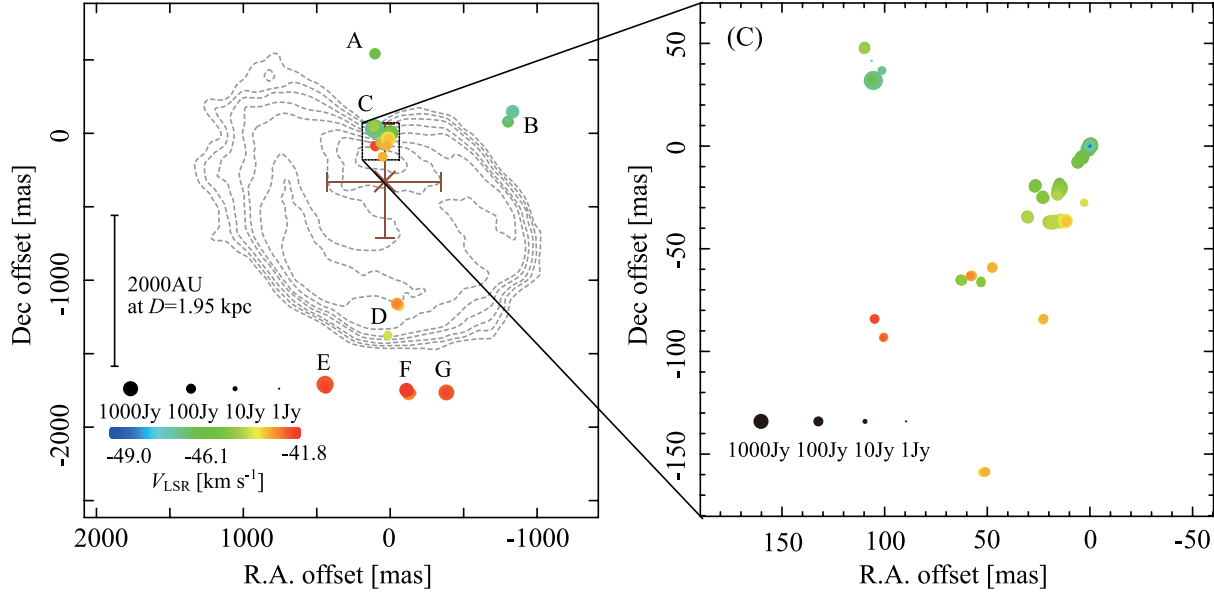
**Fig. 1.** Left: The distribution of 6.7 GHz methanol maser components. The sizes of the plotted circles are proportional to the integral flux intensities of the components which were observed on day of year (DOY) 301 in 2008 (epoch 2), on the logarithm scale. The errors in the positions of the features are smaller than the circle sizes. The color-code represents the LSR velocity. The dashed line is a 15 GHz radio continuum map of the UC H II region (Bloemhof et al. 1992). The position of the ionizing star is shown by a brown cross with error bars (Feigelson & Townsley 2008). The origin of this map is $\alpha_{J2000.0} = 02^h27^m03^s.818$, $\delta_{J2000.0} = 61°52'25''.248$. Right: Zoom-in view of the left panel around the map origin.

components extend over an area of $\sim 1''.3 \times 2''.3$. This distribution indicates that 6.7 GHz methanol masers spread more widely than in the UC H II region in the south–north direction. These methanol masers are mainly distributed in the western part of the UC H II region on the sky plane. The distribution of the 6.7 GHz methanol maser is similar to the OH maser distribution, but the 6.7 GHz methanol maser has a more patchy distribution than the 6035 MHz OH maser (see figure 1 of Fish & Sjouwerman 2007).

The most complicated velocity/spatial distribution was seen in cluster C in figure 1. Only cluster C has a wide velocity range of $\sim 6.7$ km s$^{-1}$ ($v_{LSR}$ is from $-42.2$ to $-48.9$ km s$^{-1}$). On the other hand, the other maser clusters have a narrower velocity range, being 1.2 km s$^{-1}$ or less. These trends have been basically maintained for more than 16 yr between our results and those of Menten et al. (1992). However, the velocity range of cluster C is wider than the results of Menten et al. (1992) by $\sim 2.4$ km s$^{-1}$, and there are some velocity shifts less than 1 km s$^{-1}$ for the other clusters.

Figure 2 and table 2 show internal proper motions of 107 maser components in the in-beam map. These motions were measured relative to the reference maser component with $v_{LSR} = -45.4$ km s$^{-1}$. We note that the measured internal proper motions are fairly small. In fact, in only 30 maser components were detected their proper motions with $3\sigma$ or larger values of the least-square fittings. Nearly half of the components (49 components) have proper motions equal to, or less than, $1\sigma$. Therefore, most of the proper motions of the individual components did not have high accuracies, and hence, the motions of each component may not be reliable. In addition, the variations of the maser component structures could also have some influence on the proper-motion

measurements of the components. Thus, to obtain more reliable motions, we averaged the maser proper motions with equal weighting in each maser cluster with that of A to G, and derived the relative motions of each maser cluster (A, B, D–F) to cluster C. These motions are also plotted in the bottom-left panel of figure 2 with thick black vectors. The global motions for the south–north direction were larger than those for the east–west direction. Southern maser clusters E–G show motions toward the south, and moving away from cluster C.

In the bottom-left panel of figure 2, the internal proper motions of the 1665 MHz OH maser and 15 GHz radio continuum of Bloemhof, Reid, and Moran (1992) were superposed to our results. Note that the reference component of $v_{LSR} = -43.88$ km s$^{-1}$ was used to derive the internal proper motions for OH masers in Bloemhof, Reid, and Moran (1992), while we used $v_{LSR} = -45.4$ km s$^{-1}$ for methanol masers. Therefore, there could be an unknown proper-motion offset between our results and those of Bloemhof, Reid, and Moran (1992). However, since these reference components are in the same region of cluster C, and since the difference in the systemic velocities is only $\sim 1.5$ km s$^{-1}$, the proper-motion offset is expected to be small. Actually, most of the derived internal proper motions are $\sim 3$ to 5 km s$^{-1}$, and the proper motions of the OH and methanol masers show a similar trend of expansions in figure 2, implying that the proper-motion offset is fairly small. A detailed discussion on the maser proper motion is given in subsection 4.2.

### 3.2. Parallax and Absolute Proper Motions

We detected the absolute proper motions of five maser components in cluster C based on the method described in subsection 2.4. These motions are presented in figure 3. The

**Table 2.** Detected maser components at epoch 2 and the relative proper motions.

| ID | $v_{\rm LSR}$ [km s$^{-1}$] | $X$ (error)* [mas] | $Y$ (error)* [mas] | $S^{\dagger}$ [Jy] | $v_X$ (error) [mas yr$^{-1}$] | $v_Y$ (error) [mas yr$^{-1}$] |
|---|---|---|---|---|---|---|
| 1 | −48.91 | −0.15 (0.26) | 0.28 (0.30) | 0.49 | — | — |
| 2 | −48.73 | −0.33 (0.22) | 0.39 (0.27) | 0.60 | — | — |
| 3 | −48.55 | 0.03 (0.18) | 0.07 (0.22) | 0.81 | — | — |
| 4 | −48.37 | 0.21 (0.15) | −0.14 (0.20) | 0.97 | — | — |
| 5 | −48.19 | 0.22 (0.14) | −0.24 (0.17) | 0.98 | — | — |
| 6 | −48.01 | 0.14 (0.13) | −0.19 (0.15) | 1.00 | — | — |
| 7 | −47.83 | −0.05 (0.11) | −0.08 (0.13) | 1.13 | — | — |
| 8 | −47.65 | −0.24 (0.09) | 0.13 (0.10) | 1.28 | −0.42 (0.14) | 0.30 (0.19) |
| 9 | −47.51 | −0.12 (0.08) | 0.02 (0.09) | 1.61 | −0.29 (0.12) | 0.14 (0.16) |
| 10 | −47.33 | −0.12 (0.07) | 0.10 (0.09) | 2.04 | — | — |
| 11 | −47.15 | −0.14 (0.06) | 0.15 (0.08) | 2.56 | −0.03 (0.02) | −0.30 (0.01) |
| 12 | −46.97 | −0.22 (0.05) | 0.23 (0.06) | 3.26 | −0.18 (0.04) | −0.01 (0.00) |
| 13 | −46.97 | 106.34 (0.12) | 41.56 (0.22) | 1.17 | — | — |
| 14 | −46.79 | −833.77 (0.06) | 149.00 (0.08) | 4.05 | −0.39 (0.02) | 0.03 (0.47) |
| 15 | −46.79 | −0.14 (0.04) | 0.17 (0.05) | 4.15 | −0.20 (0.00) | 0.10 (0.05) |
| 16 | −46.61 | −833.94 (0.05) | 148.81 (0.06) | 6.17 | −0.35 (0.09) | 0.02 (0.44) |
| 17 | −46.61 | −802.58 (0.18) | 79.54 (0.22) | 1.52 | — | — |
| 18 | −46.61 | −0.14 (0.03) | 0.26 (0.04) | 5.49 | −0.15 (0.05) | 0.13 (0.04) |
| 19 | −46.61 | 101.23 (0.09) | 37.28 (0.11) | 1.54 | −0.48 (0.14) | 0.13 (0.08) |
| 20 | −46.43 | −834.15 (0.10) | 148.54 (0.13) | 3.48 | — | — |
| 21 | −46.43 | −802.65 (0.13) | 79.42 (0.14) | 2.64 | −0.25 (0.17) | 0.09 (0.11) |
| 22 | −46.43 | −0.10 (0.03) | 0.18 (0.03) | 7.24 | −0.07 (0.06) | 0.08 (0.08) |
| 23 | −46.43 | 101.29 (0.05) | 36.81 (0.06) | 4.03 | −0.46 (0.15) | −0.00 (0.21) |
| 24 | −46.25 | −802.05 (0.08) | 79.24 (0.08) | 5.31 | −0.29 (0.01) | 0.27 (0.14) |
| 25 | −46.25 | −801.06 (0.10) | 89.08 (0.11) | 3.45 | — | — |
| 26 | −46.25 | −0.13 (0.03) | 0.34 (0.03) | 11.76 | −0.03 (0.14) | −0.02 (0.13) |
| 27 | −46.25 | 105.56 (0.06) | 31.95 (0.08) | 8.77 | 0.14 (0.25) | 0.61 (0.19) |
| 28 | −46.07 | −801.95 (0.02) | 79.19 (0.03) | 35.30 | −0.04 (0.05) | 0.12 (0.12) |
| 29 | −46.07 | −0.00 (0.04) | 0.24 (0.05) | 20.27 | −0.04 (0.15) | −0.02 (0.21) |
| 30 | −46.07 | 105.94 (0.04) | 32.30 (0.05) | 28.99 | −0.01 (0.00) | −0.06 (0.20) |
| 31 | −45.89 | −802.54 (0.02) | 79.44 (0.02) | 127.02 | −0.00 (0.11) | 0.14 (0.26) |
| 32 | −45.89 | −0.46 (0.02) | 0.89 (0.03) | 86.69 | 0.04 (0.09) | −0.12 (0.05) |
| 33 | −45.89 | 106.12 (0.04) | 32.45 (0.05) | 63.79 | −0.17 (0.05) | −0.09 (0.13) |
| 34 | −45.71 | −803.16 (0.04) | 79.69 (0.04) | 173.76 | 0.28 (0.28) | −0.18 (0.35) |
| 35 | −45.71 | −0.48 (0.01) | 0.83 (0.01) | 482.13 | 0.03 (0.01) | −0.10 (0.07) |
| 36 | −45.71 | 106.33 (0.05) | 32.55 (0.08) | 72.86 | −0.07 (0.11) | −0.03 (0.17) |
| 37 | −45.58 | −803.65 (0.17) | 79.53 (0.16) | 100.68 | 0.47 (0.01) | −0.17 (0.12) |
| 38 | −45.58 | −0.29 (0.01) | 0.50 (0.01) | 1163.70 | 0.04 (0.03) | −0.11 (0.08) |
| 39 | −45.40 | 0.00 (0.01) | 0.00 (0.01) | 1394.30 | −0.01 (0.01) | −0.02 (0.01) |
| 40 | −45.22 | 0.84 (0.01) | −1.44 (0.01) | 1081.00 | −0.41 (0.38) | 0.71 (0.58) |
| 41 | −45.22 | 104.08 (0.11) | 541.82 (0.08) | 157.29 | 0.71 (0.05) | −0.59 (0.22) |
| 42 | −45.22 | 26.20 (0.11) | −18.55 (0.15) | 54.58 | — | — |
| 43 | −45.04 | 3.89 (0.03) | −5.57 (0.03) | 797.09 | — | — |
| 44 | −45.04 | 14.81 (0.08) | −18.01 (0.11) | 143.33 | — | — |
| 45 | −45.04 | 22.65 (0.06) | −24.07 (0.06) | 99.50 | −0.65 (0.19) | 0.69 (0.13) |
| 46 | −45.04 | 26.44 (0.03) | −18.99 (0.03) | 206.74 | −0.26 (0.06) | 0.01 (0.01) |
| 47 | −45.04 | 103.34 (0.11) | 542.25 (0.08) | 151.09 | 0.56 (0.09) | −0.92 (0.26) |
| 48 | −44.86 | 5.84 (0.04) | −7.75 (0.03) | 428.62 | 0.16 (0.03) | −0.26 (0.08) |
| 49 | −44.86 | 14.82 (0.03) | −19.39 (0.03) | 497.38 | −0.06 (0.20) | −0.43 (0.05) |
| 50 | −44.86 | 23.07 (0.04) | −24.66 (0.04) | 242.54 | −0.43 (0.11) | 0.27 (0.01) |
| 51 | −44.86 | 26.56 (0.02) | −19.28 (0.03) | 360.44 | −0.33 (0.05) | 0.17 (0.04) |
| 52 | −44.68 | 6.07 (0.07) | −8.04 (0.07) | 162.70 | −0.08 (0.37) | −0.13 (0.37) |
| 53 | −44.68 | 14.49 (0.02) | −19.95 (0.02) | 1031.80 | −0.18 (0.20) | 0.05 (0.36) |
| 54 | −44.68 | 23.07 (0.05) | −25.06 (0.04) | 321.11 | 0.05 (0.03) | −0.23 (0.17) |

**Table 2.** (Continued)

| ID | $v_{\mathrm{LSR}}$ [km s$^{-1}$] | $X$ (error)* [mas] | $Y$ (error)* [mas] | $S^{\dagger}$ [Jy] | $v_X$ (error) [mas yr$^{-1}$] | $v_Y$ (error) [mas yr$^{-1}$] |
|---|---|---|---|---|---|---|
| 55 | −44.68 | 26.84 (0.04) | −19.63 (0.04) | 289.08 | −0.04 (0.23) | −0.07 (0.20) |
| 56 | −44.50 | 14.76 (0.01) | −20.91 (0.01) | 1229.80 | 0.53 (0.35) | −0.60 (0.31) |
| 57 | −44.50 | 19.84 (0.06) | −36.53 (0.07) | 109.34 | 0.03 (0.03) | −0.37 (0.10) |
| 58 | −44.50 | 22.54 (0.11) | −25.13 (0.06) | 245.16 | −0.24 (1.25) | 0.02 (0.74) |
| 59 | −44.50 | 53.04 (0.07) | −66.47 (0.07) | 61.74 | 0.26 (0.06) | −0.04 (0.02) |
| 60 | −44.50 | 62.91 (0.07) | −65.19 (0.07) | 140.62 | −0.50 (0.01) | −0.35 (0.20) |
| 61 | −44.50 | 109.77 (0.09) | 48.16 (0.14) | 136.96 | −0.15 (0.27) | −0.82 (0.83) |
| 62 | −44.32 | 15.14 (0.16) | −21.85 (0.17) | 832.13 | 0.96 (0.59) | −0.89 (0.56) |
| 63 | −44.32 | 19.92 (0.02) | −36.92 (0.02) | 306.00 | 0.03 (0.03) | −0.37 (0.10) |
| 64 | −44.32 | 30.56 (0.08) | −34.30 (0.07) | 266.94 | −0.28 (0.33) | 0.16 (0.18) |
| 65 | −44.32 | 53.08 (0.08) | −65.69 (0.08) | 65.43 | 0.23 (0.15) | 0.00 (0.52) |
| 66 | −44.32 | 62.27 (0.07) | −65.35 (0.07) | 126.88 | −0.56 (0.03) | −0.26 (0.04) |
| 67 | −44.32 | 109.78 (0.05) | 47.76 (0.08) | 194.26 | −0.09 (0.13) | −0.29 (0.10) |
| 68 | −44.14 | 15.74 (0.04) | −23.34 (0.04) | 366.91 | 0.42 (0.10) | −0.09 (0.10) |
| 69 | −44.14 | 19.67 (0.01) | −37.15 (0.01) | 525.46 | 0.10 (0.02) | −0.20 (0.06) |
| 70 | −44.14 | 30.26 (0.06) | −34.63 (0.05) | 272.23 | 0.36 (0.20) | 0.23 (0.07) |
| 71 | −44.14 | 110.07 (0.09) | 47.39 (0.12) | 110.11 | −0.06 (0.31) | 0.07 (0.31) |
| 72 | −43.96 | 15.88 (0.18) | −24.13 (0.18) | 90.28 | — | — |
| 73 | −43.96 | 18.88 (0.01) | −37.12 (0.01) | 738.88 | 0.22 (0.14) | −0.22 (0.14) |
| 74 | −43.96 | 30.35 (0.06) | −34.61 (0.05) | 169.74 | 0.21 (0.26) | 0.10 (0.10) |
| 75 | −43.83 | −59.71 (0.06) | −1173.12 (0.06) | 131.31 | −0.18 (0.08) | −0.08 (0.24) |
| 76 | −43.83 | 16.73 (0.10) | −1376.07 (0.08) | 67.10 | −0.17 (0.32) | −0.10 (0.19) |
| 77 | −43.83 | 17.67 (0.01) | −36.97 (0.01) | 937.46 | 0.44 (0.35) | −0.34 (0.27) |
| 78 | −43.65 | −59.03 (0.08) | −1172.85 (0.08) | 150.31 | −0.19 (0.06) | −0.12 (0.23) |
| 79 | −43.65 | 16.70 (0.10) | −1375.92 (0.10) | 48.69 | −0.27 (0.34) | −0.19 (0.09) |
| 80 | −43.65 | 2.75 (0.12) | −27.58 (0.11) | 49.55 | — | — |
| 81 | −43.65 | 14.56 (0.02) | −36.56 (0.02) | 1146.80 | — | — |
| 82 | −43.47 | −58.39 (0.12) | −1172.61 (0.12) | 76.75 | — | — |
| 83 | −43.47 | 11.96 (0.01) | −36.48 (0.01) | 757.44 | −0.50 (0.28) | 0.06 (0.00) |
| 84 | −43.29 | 11.63 (0.01) | −36.65 (0.01) | 368.31 | −0.21 (0.15) | 0.03 (0.02) |
| 85 | −43.29 | −46.62 (0.11) | −1160.45 (0.14) | 136.47 | −0.87 (0.99) | 0.17 (0.86) |
| 86 | −43.29 | 22.89 (0.06) | −84.61 (0.07) | 68.53 | −0.01 (0.07) | −0.01 (0.26) |
| 87 | −43.29 | 47.35 (0.12) | −58.95 (0.10) | 82.09 | 0.25 (0.04) | −0.45 (0.02) |
| 88 | −43.29 | 52.29 (0.09) | −158.76 (0.10) | 59.99 | −0.24 (0.32) | −0.53 (0.16) |
| 89 | −43.11 | −46.46 (0.04) | −1160.01 (0.05) | 261.46 | −0.71 (0.12) | −0.17 (0.43) |
| 90 | −43.11 | 11.49 (0.06) | −36.60 (0.05) | 88.50 | −0.22 (0.12) | −0.06 (0.02) |
| 91 | −43.11 | 22.77 (0.04) | −84.36 (0.04) | 99.62 | −0.07 (0.03) | −0.08 (0.06) |
| 92 | −43.11 | 47.60 (0.05) | −59.13 (0.04) | 121.50 | −0.08 (0.17) | −0.19 (0.07) |
| 93 | −43.11 | 51.41 (0.05) | −158.78 (0.05) | 91.06 | −0.08 (0.03) | −0.45 (0.28) |
| 94 | −43.11 | 57.37 (0.08) | −63.09 (0.05) | 95.60 | −0.12 (0.56) | −0.41 (0.21) |
| 95 | −42.93 | −117.15 (0.15) | −1772.55 (0.10) | 209.33 | −0.31 (0.61) | −1.70 (1.40) |
| 96 | −42.93 | −46.23 (0.03) | −1159.51 (0.04) | 242.09 | −0.38 (0.06) | −1.31 (0.99) |
| 97 | −42.93 | 22.53 (0.07) | −83.83 (0.08) | 61.16 | −0.06 (0.00) | −0.32 (0.17) |
| 98 | −42.93 | 47.64 (0.07) | −59.15 (0.06) | 102.32 | 0.05 (0.25) | −0.36 (0.12) |
| 99 | −42.93 | 50.72 (0.07) | −158.54 (0.07) | 63.43 | 0.04 (0.29) | −0.55 (0.42) |
| 100 | −42.93 | 57.75 (0.04) | −63.18 (0.03) | 130.93 | −0.24 (0.42) | −0.30 (0.22) |
| 101 | −42.75 | −126.13 (0.23) | −1772.10 (0.04) | 15.76 | — | — |
| 102 | −42.75 | −125.42 (0.12) | −1771.48 (0.04) | 453.07 | — | — |
| 103 | −42.75 | −46.00 (0.05) | −1158.76 (0.08) | 126.98 | −0.34 (0.02) | −1.76 (1.36) |
| 104 | −42.75 | 58.31 (0.05) | −63.35 (0.04) | 71.79 | −0.26 (0.03) | −0.27 (0.08) |
| 105 | −42.75 | 100.32 (0.06) | −92.88 (0.06) | 47.87 | −0.01 (0.08) | −0.34 (0.28) |
| 106 | −42.57 | −152.49 (0.07) | −1766.63 (0.07) | 35.99 | −0.11 (0.04) | −0.69 (0.34) |
| 107 | −42.57 | −131.92 (0.03) | −1771.01 (0.02) | 173.14 | 0.85 (0.62) | −0.50 (0.16) |
| 108 | −42.57 | −131.02 (0.11) | −1741.71 (0.10) | 34.73 | — | — |

**Table 2.** (Continued)

| ID | $v_{\mathrm{LSR}}$ [km s$^{-1}$] | $X$ (error)* [mas] | $Y$ (error)* [mas] | $S^{\dagger}$ [Jy] | $v_X$ (error) [mas yr$^{-1}$] | $v_Y$ (error) [mas yr$^{-1}$] |
|---|---|---|---|---|---|---|
| 109 | −42.57 | −123.30 (0.05) | −1771.66 (0.03) | 109.53 | −0.78 (0.25) | −0.23 (0.23) |
| 110 | −42.57 | −45.78 (0.09) | −1157.94 (0.16) | 35.59 | — | — |
| 111 | −42.57 | 58.46 (0.08) | −63.09 (0.09) | 16.63 | −0.28 (0.05) | −0.39 (0.40) |
| 112 | −42.57 | 100.49 (0.02) | −93.17 (0.02) | 60.67 | −0.14 (0.03) | −0.09 (0.15) |
| 113 | −42.39 | −152.19 (0.13) | −1766.30 (0.10) | 12.97 | — | — |
| 114 | −42.39 | −129.11 (0.04) | −1771.26 (0.02) | 138.49 | — | — |
| 115 | −42.39 | −124.47 (0.03) | −1771.69 (0.02) | 111.82 | 0.21 (0.39) | −0.31 (0.26) |
| 116 | −42.39 | −122.59 (0.12) | −1747.16 (0.11) | 26.18 | 0.23 (0.40) | −0.47 (1.17) |
| 117 | −42.39 | 100.65 (0.02) | −93.32 (0.02) | 39.43 | −0.12 (0.00) | −0.10 (0.06) |
| 118 | −42.39 | 104.69 (0.08) | −83.68 (0.10) | 20.55 | −0.21 (0.18) | −1.24 (0.47) |
| 119 | −42.21 | −382.81 (0.13) | −1763.92 (0.11) | 7.26 | — | — |
| 120 | −42.21 | −126.15 (0.10) | −1771.63 (0.05) | 26.04 | −0.46 (2.77) | −0.08 (0.56) |
| 121 | −42.21 | −121.50 (0.07) | −1748.08 (0.06) | 16.68 | 0.25 (0.12) | −0.61 (0.43) |
| 122 | −42.21 | −111.44 (0.06) | −1747.45 (0.05) | 14.87 | −0.43 (0.01) | −0.09 (0.02) |
| 123 | −42.21 | 100.82 (0.03) | −93.45 (0.03) | 11.21 | −0.07 (0.02) | −0.10 (0.06) |
| 124 | −42.21 | 104.76 (0.04) | −83.84 (0.05) | 14.85 | −0.06 (0.06) | −0.87 (0.19) |
| 125 | −42.21 | 443.52 (0.06) | −1710.07 (0.07) | 7.88 | 0.10 (0.20) | −0.84 (0.05) |
| 126 | −42.03 | −382.93 (0.20) | −1763.80 (0.16) | 4.08 | −0.02 (0.05) | −0.52 (0.31) |
| 127 | −42.03 | −120.25 (0.13) | −1748.64 (0.10) | 5.13 | — | — |
| 128 | −42.03 | −111.36 (0.04) | −1747.38 (0.03) | 15.39 | −0.19 (0.12) | −0.20 (0.11) |
| 129 | −42.03 | 104.88 (0.07) | −84.16 (0.08) | 4.48 | −0.03 (0.19) | −0.69 (0.10) |
| 130 | −42.03 | 437.76 (0.05) | −1730.94 (0.07) | 5.46 | 0.23 (0.02) | −0.61 (0.16) |
| 131 | −42.03 | 443.43 (0.08) | −1709.35 (0.10) | 3.94 | 0.04 (0.04) | −1.27 (0.59) |
| 132 | −41.89 | −111.14 (0.06) | −1747.47 (0.05) | 6.54 | −0.31 (0.28) | −0.09 (0.02) |
| 133 | −41.89 | 437.75 (0.06) | −1730.94 (0.05) | 10.36 | 0.21 (0.04) | −0.61 (0.13) |
| 134 | −41.71 | 437.66 (0.03) | −1731.10 (0.04) | 6.87 | 0.23 (0.01) | −0.56 (0.15) |
| 135 | −41.53 | 437.66 (0.09) | −1731.63 (0.11) | 1.70 | — | — |

\* $X$ and $Y$ are the position offsets from the reference maser component (ID: 39) toward the east and the north, respectively.
$^{\dagger}$ Integral flux intensities of the components.

fitting results with annual parallax and the absolute proper motions are also shown in figures 3 and 4 and listed in tables 3 and 4. From the fitting with three maser components (3a–3c) supposed 100% correlation, the annual parallax $\pi$ was $0.598 \pm 0.067$ (error : 11%) mas for 6.7 GHz methanol maser toward W 3(OH). This parallax corresponds to a distance of $1.67^{+0.21}_{-0.17}$ kpc from the Sun. This parallax and error amplitude are larger than the previous results (Xu et al. 2006; Hachisuka et al. 2006), as discussed in detail in subsection 4.1.

The standard deviations of the post-fit residuals, which were determined so that the reduced $\chi^2$ would become unity, were found to be $\sigma_\alpha = 0.49$ mas in right ascension and $\sigma_\delta = 0.17$ mas in declination. These residuals are likely to represent the positional uncertainties in the present astrometric observations. These residuals are larger than the errors determined by dynamic ranges of maps for each maser component, which can be estimated to be $0.54\theta_{\mathrm{beam}}/SNR$ (Reid et al. 1988), corresponding to 0.03–0.22 mas for right ascension and 0.04–0.22 mas for declination in our data. For the maps of the reference source, the maximum value of $0.5\theta_{\mathrm{beam}}/SNR$ became $\sim 0.05$ mas. These residuals most likely originate in atmospheric zenith delay residuals and/or the variability of the structure of the maser components (as examples of detailed discussions, see Honma et al. 2007 and Hirota et al. 2008).

In our results, it is unusual that the residual value of right ascension is larger than the value of declination. This result could be attributed to a large position offset in the third epoch (2009/143), as can be seen in figure 4. Thus, probably the large residual in right ascension is affected by the outliers in the third epoch. However, to be conservative, we take the results including the 3rd epoch.

## 4. Discussion

### 4.1. Astrometry with JVN/VERA

Our parallax value of $\pi = 0.598 \pm 0.067$ mas is almost consistent with that of Xu et al. (2006) of $\pi = 0.512 \pm 0.010$ mas and Hachisuka et al. (2006) of $\pi = 0.489 \pm 0.017$ mas. Although our value is out of the ranges of the parallax errors of Xu et al. (2006) and Hachisuka et al. (2006), their parallaxes are only within the ranges of our errors of $1.3\sigma$ and $1.6\sigma$, respectively. Thus, the differences between our value and their ones are not statistically significant. Our parallax is systematically larger than that of Xu et al. (2006) or Hachisuka et al. (2006), which may be caused by some maser structures (possibly due to the larger beam size of our observations at 6.7 GHz) or some systematic errors (most likely caused by the ionospheric
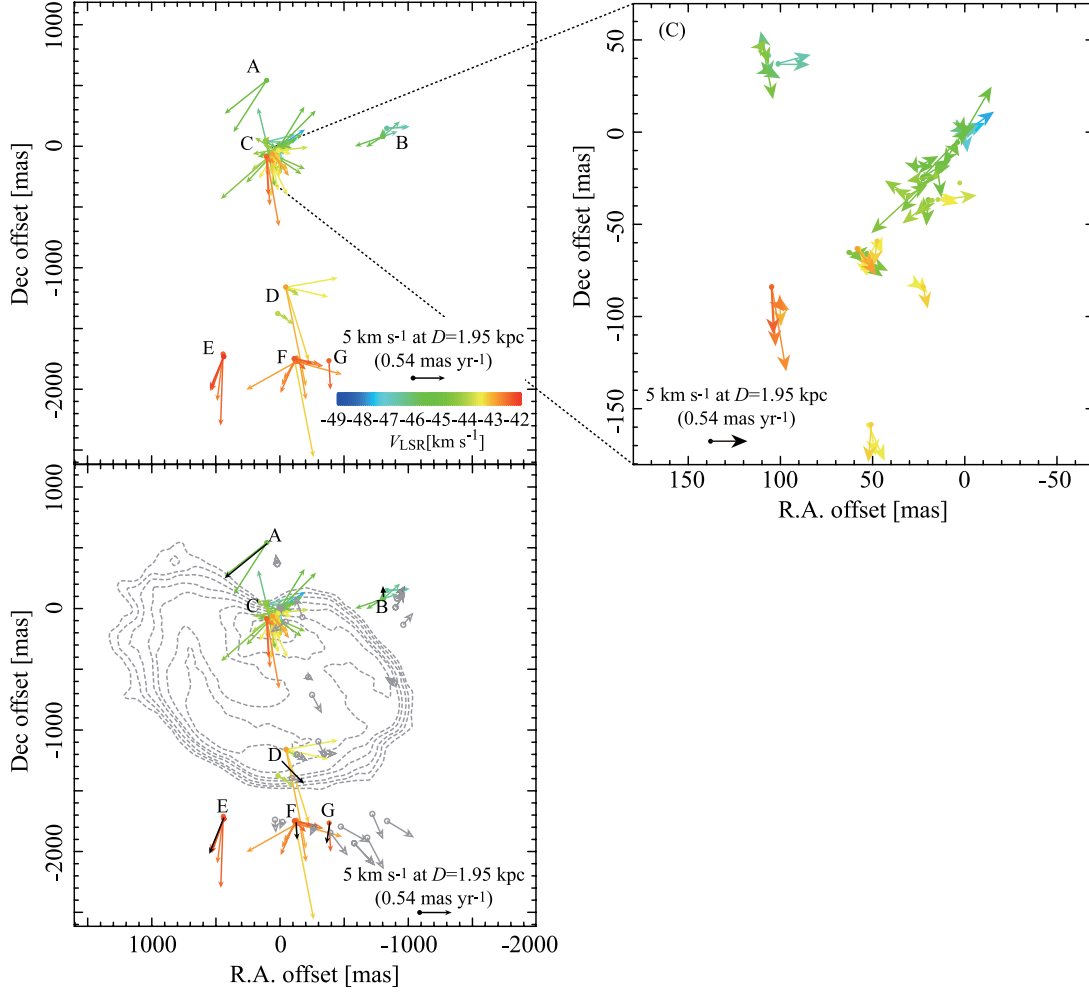
**Fig. 2.** Left: Internal proper motion for 6.7 GHz methanol maser components toward W 3(OH). Color-codes represent the LSR velocity. The colored vectors show the directions and amplitudes of the relative proper motions on the sky plane to the reference component with the $-45.4 \, \mathrm{km \, s^{-1}}$ LSR velocity. The scale of the vector is presented by a black-colored thin vector. Right: Zoom-in view of left panel around the origin. Bottom-left: The colored vectors are the same as the top-left one. The thick black vectors show the averaged relative proper motion at each cluster of A, B, and D–G to the C cluster around the origin. The proper motion vectors of 1665 MHz OH maser and the contour map of 15 GHz radio continuum emission of the UC H II region taken from figure 7 of Bloemhof, Reid, and Moran (1992) are also shown as outlined gray vectors and broken lines, respectively.

effect) which happen to increase the amplitude of the parallax. In figures 1 and 2, we adopted the most accurate distance of Xu et al. (2006). On the other hand, although we did not use the same maser components as Xu et al. (2006), our average proper motion is consistent with that of Xu et al. (2006) within their errors. The average proper motions of our results are $\mu_\alpha \cos\delta = -1.16 \pm 0.24 \, \mathrm{mas \, yr^{-1}}$ and $\mu_\delta = -0.11 \pm 0.30 \, \mathrm{mas \, yr^{-1}}$. In Xu et al. (2006), the averaged absolute proper motions for nine components are $\mu_\alpha \cos\delta = -1.204 \pm 0.02 \, \mathrm{mas \, yr^{-1}}$ and $\mu_\delta = -0.147 \pm 0.01 \, \mathrm{mas \, yr^{-1}}$. This comparison also ensures that our astrometric results are reliable, and do not include large systematics exceeding the error of the averaged proper motion.

The error of parallax with JVN/VERA is about seven or four times larger than that of Xu et al. (2006) or Hachisuka et al. (2006). The main reason for this error difference is thought to be the difference in the baseline length and the observational frequency. Both Xu et al. (2006) and Hachisuka

et al. (2006) based their results on observations with VLBA. The maximum baseline length of JVN/VERA is 2300 km. This length is $\sim 0.27$ times that of VLBA. If the accuracies in the phase calibration are the same, the astrometric accuracy is determined by the baseline length. Thus, in such a case the error of parallax for JVN/VERA simply becomes 3.7 times the error of VLBA. Moreover, our observational frequency was 6.7 GHz, while the frequency in Xu et al. (2006) was 12 GHz and in Hachisuka et al. (2006) it was 22 GHz. Therefore, our beam size in the synthesis image is $\sim 7$–12 times larger than that of Xu et al. (2006) and Hachisuka et al. (2006) in the worst case. If the phase-referenced map has a low signal-to-noise ratio, the astrometric accuracy would be determined by the beam size. Thus, the error of parallax with JVN/VERA can be 7–12 times the error of Xu et al. (2006) and Hachisuka et al. (2006). Also, if there are some structures in the maser components, astrometric results can be more influenced by a larger beam. In addition, the effects of the ionosphere are also larger
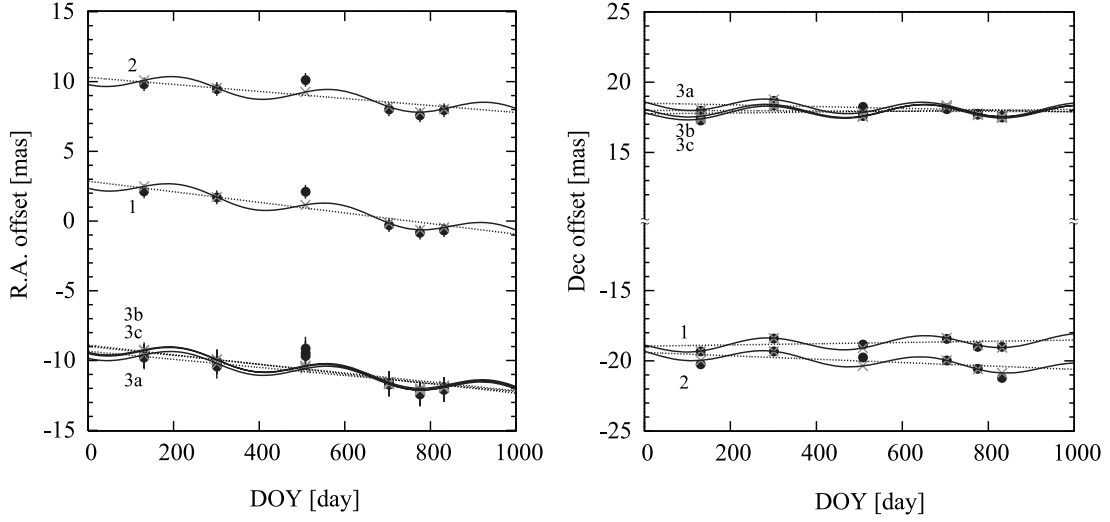
**Fig. 3.** Results of fitting the parallax with the absolute proper motions. Labels of 1, 2, 3a, 3b, and 3c correspond to the LSR velocity $v_{LSR} = -43.10$, $-43.80$, $-45.91$, $-45.20$, and $-45.60\,km\,s^{-1}$, respectively. Left: The movement in right ascension as a function of time. The first day is New Year's day 2008. Black circles and vertical bars represent the position offsets of the components and fitting weights, respectively. Gray ×-marks represent the ideal position offsets of the components on the least-square fitting. Broken lines and solid lines represent the results of the least-square fitting of absolute proper motions for the components, and the absolute proper motions modulated by the annual parallax, respectively. Right: The same as the left panel in declination. For details refer to tables 3 and 4.
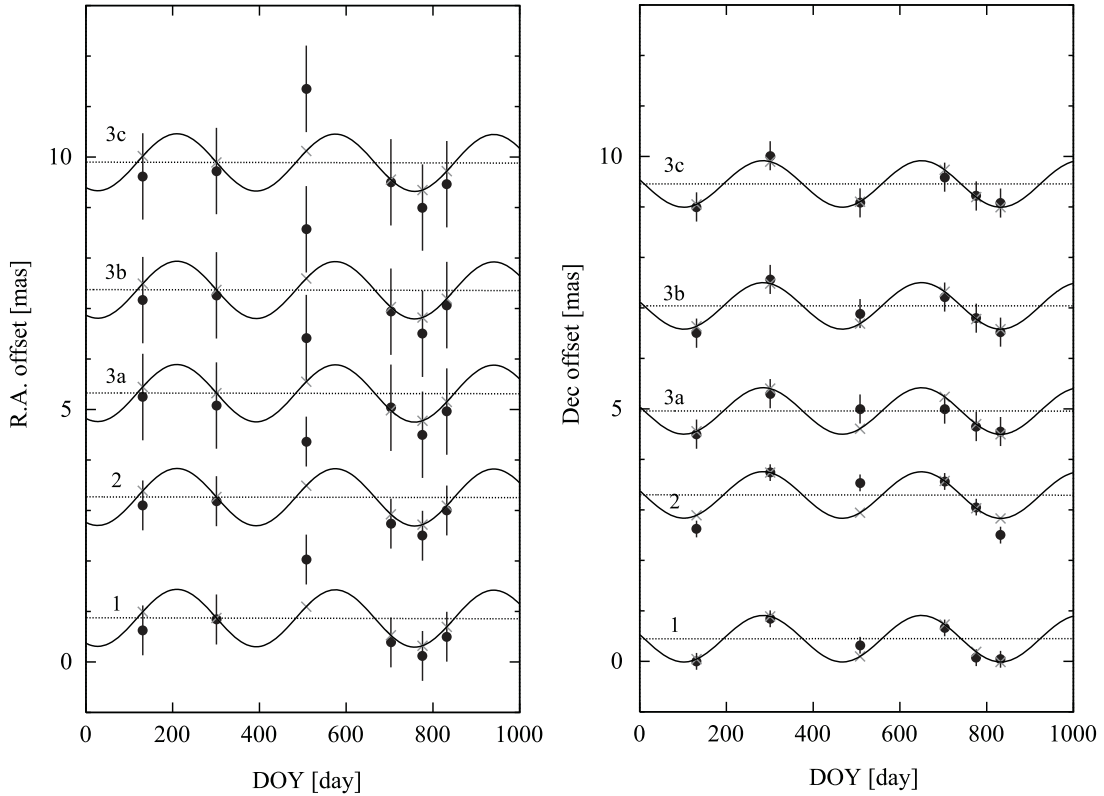


**Fig. 4.** Results of positional offsets variation for the maser components of $v_{LSR} = -43.10$ (1), $-43.80$ (2), $-45.91$ (3a), $-45.20$ (3b), and $-45.60$ (3c) $km\,s^{-1}$ after subtracting the best-fit proper motions. Left: The movement in right ascension as a function of time. The first day corresponds to New Year's day 2008. Black circles represent the position offsets of the components with vertical bars of fitting weights. Gray ×-marks represent the ideal position offsets of the components on the least-square fitting. The solid lines and broken lines represent the modulation in the positions due to the annual parallax, and the results of subtracting the best-fit absolute proper motions for the components, respectively. Right : The same as the left panel in declination. For details refer to tables 3 and 4.

**Table 3.** Parallax and absolute proper motion fittings.

| ID | $\Delta\alpha\cos\delta^*$ [mas] | $\Delta\delta^*$ [mas] | $v_{\mathrm{LSR}}$ [km s$^{-1}$] | Epochs used for fitting | $F_{\mathrm{peak}}$ [Jy beam$^{-1}$] | | SNR | $\mu_\alpha\cos\delta$ [mas yr$^{-1}$] | $\mu_\delta$ [mas yr$^{-1}$] |
|---|---|---|---|---|---|---|---|---|---|
| 1 | 2.13 | −19.35 | −43.10 | 123456 | 53 | −181 | 18–43 | −1.39 ± 0.32 | 0.16 ± 0.13 |
| 2 | 9.81 | −20.23 | −43.80 | 123456 | 57 | −241 | 18–32 | −0.92 ± 0.32 | −0.44 ± 0.13 |
| 3a[†] | −9.78 | 17.97 | −45.91 | 123456 | 10 | −178 | 13–51 | −1.06 ± 0.32 | −0.23 ± 0.13 |
| 3b[†] | −9.55 | 17.25 | −45.20 | 123456 | 104 | −423 | 19–44 | −1.26 ± 0.32 | 0.12 ± 0.13 |
| 3c[†] | −9.68 | 17.53 | −46.60 | 123456 | 0.9– | 41 | 12–51 | −1.16 ± 0.32 | −0.03 ± 0.13 |
| Average of 3a–3c | | | | | | | | −1.16 ± 0.18 | −0.05 ± 0.08 |
| Average in above three maser features (Standard deviation) | | | | | | | | −1.16 (0.24) | −0.11 (0.30) |

* The relative coordinates to the phase center at epoch 1.
† Spots in the same maser feature.

**Table 4.** Parallax and absolute proper-motion fittings.

| | |
|---|---|
| Parallax $\pi$ [mas] | 0.598 ± 0.067 |
| Distance $D$ [kpc] | $1.67^{+0.21}_{-0.17}$ |
| $\sigma_\alpha$ [mas] | 0.49 |
| $\sigma_\delta$ [mas] | 0.17 |

at lower frequency. Given the discussions described above, our results are fairly reasonable when compared with those obtained with the VLBA. Thus, we conclude that JVN/VERA is able to conduct astrometry for sources within a few kpc.

VERA is an array dedicated to astrometry, and capable of observing many sources routinely. In addition, combinations of large telescopes in JVN (e.g., Usuda 64 m and Yamaguchi 32 m telescopes) dramatically improve the sensitivity of the array. Also, in the near future, JVN/VERA will expand to East Asia VLBI Network (EAVN), including stations in Korea and China, providing a longer, up to ∼ 6000 km baseline and hence better accuracy. On the other hand, VLBA can only observe methanol maser sources at 12 GHz now, and European VLBI Network has only three sessions per year for the observation of 6.7 GHz methanol maser. We note that 6.7 GHz methanol maser sources are now becoming more important in studying the structure of the Galaxy with VLBI astrometry (e.g., measuring the spiral structure and galactic rotation: Rygl et al. 2010), because the 6.7 GHz methanol maser is bright and stationary, and a large number of sources have already been discovered in the galactic plane, as noted in section 1. Therefore, JVN/VERA (and EAVN in the near future) can play an important role in the VLBI astrometry of the Galaxy through observations of 6.7 GHz methanol masers.

### 4.2. Structure of Maser Emitting Region

Based on previous observations, the structure of the W 3(OH) region showed the following characteristics: (i) The ammonia absorption lines are associated with the western part of the UC H II region. The NH$_3$ (2, 2) absorption line of W 3(OH) suggests that the molecular gas is located in front of the toruslike structure overlying the UC H II region with north–south extension (Guilloteau et al. 1983). They suggest that the back side of the torus cannot be observed, because the UC H II region is optically thick at this wavelength (Dreher

& Welch 1981). (ii) OH maser emissions are more clumpy than the absorption line of molecular gas traced with NH$_3$, but also show continuous distributions along the ammonia absorption line (e.g., Fish & Sjouwerman 2007; Harvey-Smith & Cohen 2006, 2005; Wright et al. 2004a, 2004b; Menten et al. 1992). The velocities and spatial distributions are basically similar to the 6.7 GHz methanol maser (Harvey-Smith & Cohen 2006; Menten et al. 1992). (iii) North–south expansion was seen in the internal proper motion of the 1665 MHz OH maser (Wright et al. 2004a; Bloemhof et al. 1992). In addition, in the 1667 MHz OH maser (Wright et al. 2004b), there are several arc structures, which were suggested to be shock fronts caused by interacting with the expanding UC H II region. (iv) The velocity gradient in the north–south direction was seen in the 1665 MHz OH maser (Wright et al. 2004a), which implies rotation from north to south. On the other hand, Fish and Sjouwerman (2007) suggest a rotation of which direction is opposite from that suggested by Wright et al. (2004a). The opposite direction of rotation is based on their internal proper motions and on newly detected blue-shifted components in the southeast of the 6035 MHz OH maser. Thus, there is a disagreement in the rotational direction between these observations of the OH maser. These differences in the rotational direction based on the internal proper motion could be dependent on the interpretation of the complicated velocity structure of the maser clusters. In any case, the structure of NH$_3$ absorption and OH masers indicates a torus with expansion and clockwise or counter-clockwise rotation.

On the other hand, as can be seen in figure 1, our data suggest that the 6.7 GHz methanol maser components are only distributed in the western part of the UC H II region in our data. The blue-shifted components are mostly located in the northern part, and the red-shifted components are located in the southern part. About the internal proper motions, the separations between cluster C and southern clusters (D–F) increase over time, as can be seen in figure 2. This trend suggests north–south expansion. This sense is consistent with the OH maser motions obtained by Bloemhof, Reid, and Moran (1992) and Wright, Gray, and Diamond (2004a). Here, if this expansion is an outflow, maser components belong to the outflow, and are not necessarily consistent with the UC H II region. However, there exists a maser component concentration associated with the "pinch" of the UC H II region (cluster C) — which could be caused by a denser clump in the outlying gas which suppresses
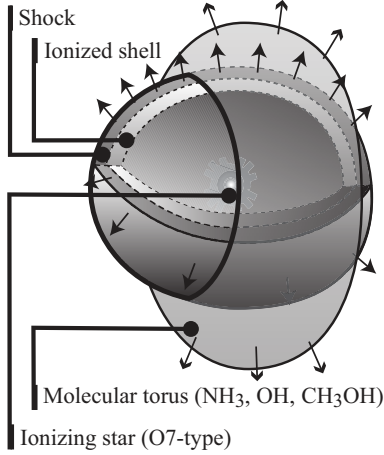
**Fig. 5.** Possible model of the W 3(OH) region. The UC H II region is expanding and has shell structure as described in Dreher and Welch (1981). Several maser emissions and NH₃ absorption come from the molecular torus out of the UC H II region. Only the front of the torus can be observed because the UC H II region is optically thick at those wavelengths. The molecular torus expands with the expansion of the UC H II region.

the expansion of the UC H II region, as suggested by Wright, Gray, and Diamond (2004a). This fact suggests a relation between the maser clouds and the expanding UC H II region. Also, we note that the typical expansion velocity of the 6.7 GHz methanol maser in figure 2 is consistent with that of the UC H II region, $3$–$5\,\mathrm{km\,s^{-1}}$ (Kawamura & Masson 1998). Therefore, our results favor the expanding torus scenario proposed earlier, whose schematic view is shown in figure 5.

The torus model can also naturally explain the excitation of the 6.7 GHz methanol maser. The 6.7 GHz methanol maser is thought to be excited by infrared photons emitted from dusts at the temperature of around 100–200 K (e.g., De Buizer et al. 2000; Sugiyama et al. 2008a). In the expanding torus model, we can estimate the dust temperature by assuming an equilibrium of energies absorbed and reemitted by dusts. In this estimation, we simply suppose that dust in the torus is warmed by the central star and reradiates as a black body with a temperature of $T_{\mathrm{dust}}$. Under such an assumption, we can express the temperature of the dust as a function of the radial distance from the ionizing star by using the Stefan–Boltzmann law,

$$4\pi\sigma r^2 T_{\mathrm{dust}}^4 = \frac{\pi r^2}{4\pi R^2} L_*. \tag{1}$$

The left side of equation (1) is the luminosity emitted by spherical dust with a radius of $r$, and the right side is the energy received by the dust from the central star. We also note that $L_*$ is the total luminosity of the ionizing star, $\sigma$ the Stefan–Boltzmann constant, and $R$ the torus radius. From this equation, the dust temperature $T_{\mathrm{dust}}$ can written as

$$T_{\mathrm{dust}} = \frac{1}{2}\left(\frac{L_*}{\pi\sigma R^2}\right)^{\frac{1}{4}}. \tag{2}$$

Taking that $L_*$ is $10^5\,L_\odot$ from the infrared luminosity by Harper (1974), and the radius $R$ is 2000 AU from the 6.7 GHz

methanol maser distribution in figure 1, we obtain $T_{\mathrm{dust}}$ is $\sim 110\,\mathrm{K}$. This estimation is consistent with other researches reporting a dust temperature of 111 K (Campbell et al. 1989). Thus, the expanding torus model can also explain the dust temperature that is most suitable for methanol maser excitation. Therefore, the torus model can reasonably explain the observed physical properties including the distributions, proper motions, and excitations of methanol masers.

We also note other possible models for W 3(OH). A disk model suggested by Wright, Gray, and Diamond (2004a) is similar to the our torus model, and so this could be another possible interpretation. Concerning a smaller scale disk model, proposed by Moscadelli, Xu, and Chen (2010) (cluster C region in our figure 1), highly accurate proper motions are crucial in their model fitting. Our data show that the systemic velocities/positions of methanol maser components at 6.7 GHz are completely consistent with their data of a 12 GHz methanol maser. However, their proper motions have 10 times better accuracy than our data, and thus it is difficult to verify their model with our observations. The reason for the difference in proper-motion accuracy is mainly the time span of the observations; while our data span was $\sim 1\,\mathrm{yr}$, their observations ranged over $\sim 10\,\mathrm{yr}$. In order to test the model proposed by Moscadelli, Xu, and Chen (2010), high-resolution continuum observations in the future may be a key to the check on the existence of some low/intermediate mass stars. Finally, we also refer to the cometary model. In addition to an expansion model, Bloemhof, Reid, and Moran (1992) also suggested a cometary bow-shock model as another possibility based on OH maser proper motions. However, recent observations of the morphology of the UC H II region have not suggested such a structure as theoretical cometary models (e.g., Arthur & Hoare 2006). Instead, Kawamura and Masson (1998) showed the expansion of the UC H II region directly. Thus, even if there is some weak cometary structure, the expanding trend should be dominant.

## 5. Conclusion

We have presented the results of multiepoch VLBI astrometry with JVN/VERA for the 6.7 GHz methanol maser associated with W 3(OH). We derived an annual parallax of W 3(OH) with the five maser components to be $0.598 \pm 0.067\,\mathrm{mas}$, corresponding to a distance of $1.67^{+0.21}_{-0.17}\,\mathrm{kpc}$ from the Sun. The absolute proper motions were also measured for the five maser components. These are the first results of JVN/VERA astrometry for 6.7 GHz methanol maser sources.

The internal proper motions of 6.7 GHz methanol masers toward W 3(OH) were also obtained. The motions of the tendency to expand are similar to previous 1.6 GHz OH maser observations by Bloemhof, Reid, and Moran (1992) and Wright, Gray, and Diamond (2004a), and favor a rotating and expanding torus structure surrounding the UC H II region.

# References

Arthur, S. J., & Hoare, M. G. 2006, ApJS, 165, 283
Campbell, M. F., Lester, D. F., Harvey, P. M., & Joy, M. 1989, ApJ, 345, 298
Chikada, Y., Kawaguchi, N., Inoue, M., Morimoto, M., Kobayashi, H., & Mattori, S. 1991, in Frontiers of VLBI, ed. H. Hirabayashi et al. (Tokyo: Universal Academy Press), 79
Baudry, A., Herpin, F., & Lucas, R. 1998, A&A, 335, 654
Baudry, A., Menten, K. M., Walmsley, C. M., & Wilson, T. L. 1993, A&A, 271, 552
Bloemhof, E. E., Reid, M. J., & Moran, J. M. 1992, ApJ, 397, 500
De Buizer, J. M., Piña, R. K., & Telesco, C. M. 2000, ApJS, 130, 437
Desmurs, J. F., Baudry, A., Wilson, T. L., Cohen, R. J., & Tofani, G. 1998, A&A, 334, 1085
Dickel, H. R., & Goss, W. M. 1987, A&A, 185, 271
Dreher, J. W., & Welch, W. J. 1981, ApJ, 245, 857
Etoka, S., Cohen, R. J., & Gray, M. D. 2005, MNRAS, 360, 1162
Feigelson, E. D., & Townsley, L. K. 2008, ApJ, 673, 354
Fish, V. L., Brisken, W. F., & Sjouwerman, L. O. 2006, ApJ, 647, 418
Fish, V. L., & Sjouwerman, L. O. 2007, ApJ, 668, 331
Green, J. A., et al. 2009, MNRAS, 392, 783
Guilloteau, S., Stier, M. T., & Downes, D. 1983, A&A, 126, 10
Hachisuka, K., et al. 2006, ApJ, 645, 337
Harper, D. A. 1974, ApJ, 192, 557
Harvey-Smith, L., & Cohen, R. J. 2005, MNRAS, 356, 637
Harvey-Smith, L., & Cohen, R. J. 2006, MNRAS, 371, 1550
Hirota, T., et al. 2008, PASJ, 60, 961
Honma, M., et al. 2007, PASJ, 59, 889
Honma, M., Tamura, Y., & Reid, M. J. 2008, PASJ, 60, 951

Kawamura, J. H., & Masson, C. R. 1998, ApJ, 509, 270
Menten, K. M., Reid, M. J., Pratap, P., Moran, J. M., & Wilson, T. L. 1992, ApJ, 401, L39
Moscadelli, L., Menten, K. M., Walmsley, C. M., & Reid, M. J. 1999, ApJ, 519, 244
Moscadelli, L., Menten, K. M., Walmsley, C. M., & Reid, M. J. 2002, ApJ, 564, 813
Moscadelli, L., Xu, Y., & Chen, X. 2010, ApJ, 716, 1356
Norris, R. P., Booth, R. S., & Diamond, P. J. 1982, MNRAS, 201, 209
Reid, M. J., Haschick, A. D., Burke, B. F., Moran, J. M., Johnston, K. J., & Swenson, G. W., Jr. 1980, ApJ, 239, 89
Reid, M. J., Myers, P. C., & Bieging, J. H. 1987, ApJ, 312, 830
Reid, M. J., Schneps, M. H., Moran, J. M., Gwinn, C. R., Genzel, R., Downes, D., & Rönnäng, B. 1988, ApJ, 330, 809
Rygl, K. L. J., Brunthaler, A., Reid, M. J., Menten, K. M., van Langevelde, H. J., & Xu, Y. 2010, A&A, 511, A2
Sugiyama, K., Fujisawa, K., Doi, A., Honma, M., Isono, Y., Kobayashi, H., Mochizuki, N., & Murata, Y. 2008a, PASJ, 60, 1001
Sugiyama, K., Fujisawa, K., Doi, A., Homna, M., Kobayashi, H., Bushimata, T., Mochizuki, N., & Murata, Y. 2008b, PASJ, 60, 23
Wright, M. M., Gray, M. D., & Diamond, P. J. 2004b, MNRAS, 350, 1253
Wright, M. M., Gray, M. D., & Diamond, P. J. 2004a, MNRAS, 350, 1272
Xu, Y., Reid, M. J., Zheng, X. W., & Menten, K. M. 2006, Science, 351, 54